Carbon 124 (2017) 23–33

Contents lists available at ScienceDirect

Carbon

journal homepage: www.elsevier.com/locate/carbon

Nitrogen and oxygen dual-doped hollow carbon nanospheres derived from catechol/polyamine as sulfur hosts for advanced lithium sulfur batteries

Yueying Peng [a], Yiyong Zhang [a], Jianxing Huang [a], Yunhui Wang [a], He Li [a], Bing Joe Hwang [b], Jinbao Zhao [a, *]

[a] State Key Lab of Physical Chemistry of Solid Surfaces, Collaborative Innovation Centre of Chemistry for Energy Materials, State-Province Joint Engineering Laboratory of Power Source Technology for New Energy Vehicle, College of Chemistry and Chemical Engineering, Xiamen University, Xiamen, 361005, PR China

[b] NanoElectrochemistry Laboratory, Department of Chemical Engineering, National Taiwan University of Science and Technology, Taipei, 106, Taiwan

ARTICLE INFO

Article history:
Received 17 May 2017
Received in revised form
18 August 2017
Accepted 19 August 2017
Available online 22 August 2017

ABSTRACT

Although lithium-sulfur batteries are considered as promising high-energy-storage system owing to their high energy density, developing effective materials to host sulfur species on the cathode is still challenging. Herein, an inexpensive and effective carbon precursor, catechol and polyamine is explored to fabricate nitrogen/oxygen dual-doped hollow carbon nanospheres (DHCSs) as sulfur hosts. The group containing nitrogen and oxygen can provide stronger chemisorption for lithium polysulfides than single-doped carbon matrix, which is confirmed by X-ray photoelectron spectroscopy analysis and the theoretical calculation. As a result, the designed sulfur/DHCSs cathode delivers a stable cycling performance remained 851 mAh g^{-1} discharge capacity at 0.2 C with ~0.08% capacity decay per cycle after 200 cycles, revealing its great promise for energy storage application.

1. Introduction

To develop high-energy storage system, much attention has been paid to lithium-sulfur (Li–S) batteries, owing to their high theoretical specific capacity (1675 mAh g^{-1}) and theoretical energy density (2600 Wh kg^{-1}) [1,2]. Moreover, elemental sulfur is environmentally friendly and inexpensive as sulfur is abundant on earth (3%, mass) [3]. In spite of these appealing advantages, there are still some severe problems plaguing the commercial application of Li–S batteries: (1) The high resistance of both sulfur ($\sigma = 5 \times 10^{-30}$ S cm^{-1} at 25 °C) and its discharged products (Li_2S_2/Li_2S). (2) The high dissolution and shuttle effect of polysulfides (Li_2S_x, $3 \leq x \leq 8$) in organic electrolyte. The lithium polysulfides (LiPSs), generated on the cathode, can readily migrate to the anode where they can react with lithium metal to produce insoluble Li_2S and Li_2S_2, causing the loss of active material sulfur. (3) The adverse volume expansion (~80%) of sulfur during discharge and charge. In consequence, Li–S batteries undergo low utilization of active materials, poor rate capability, reduced coulombic efficiency and pronounced capacity fading.

To address the above mentioned issues, much work has been carried out, especially focusing on the sulfur-carbon composites. A major breakthrough is made by Nazar's group through adopting ordered carbon to suppress polysulfide dissolution [4]. Inspired by their pioneering work, various carbon materials with unique structure, including graphene, hollow carbon spheres, carbon nanotube and carbon nanofibers have been reported to confine sulfur species by providing physical confinement [5–8]. However, continuous capacity decay, especially for long cycling is often observed in such sulfur-carbon hybrids. It has been demonstrated that it is due to the poor affinity of non-polar carbon materials with polar LiPSs, leading to continual dissolution of LiPSs into electrolytes [9]. Therefore, physical confinement alone is not enough to encapsulate soluble LiPSs, the strong chemical interaction with LiPSs is needed to effectively confine LiPSs on the cathode [10].

Doping heteroatoms into carbon substrates is a feasible way to adjust the nonpolar property of carbon materials. Along this line, various heteroatoms, such as nitrogen (N), oxygen (O) and boron

* Corresponding author.
E-mail address: jbzhao@xmu.edu.cn (J. Zhao).

http://dx.doi.org/10.1016/j.carbon.2017.08.035
0008-6223/

(B), have been reported to modify carbon substrate [11–13]. The doped atoms can trap sulfur species through bonding with positive Li^+ (e.g. N···Li_2S_n) or interacting with anion PSs (Li_2S_n···B). However, the content of single-heteroatom is generally limited [14]. Thus, dual-doping strategy is proposed to provide enough active sites for chemisorption. It is exciting to find that the dual-doped carbon exhibits improved chemisorption for LiPSs [15–18]. Recently, dual-doped carbon materials are not only limited in Li–S systems, but also in various fields, such as electrocatalysts and supercapacitor [19,20]. However, different precursors with separated steps are normally needed to achieve the incorporation of different atoms, leading heterogeneous distribution of dopants. For example, typical process with air atmosphere oxidation and subsequent nitridation treatment in concentrated HNO_3 is used to obtain N/O co-doped carbon materials [21]. In addition, strict reaction conditions, such as surface active agents or hydrothermal method, are used to fabricate doped carbon materials [18,20]. As carbon precursor plays a vital role on both physical and chemical characteristics of the final obtained carbonaceous materials [22,23], it is important to explore a universal and facile raw materials to prepared heteroatoms-doped carbon. Dopamine, benefited from its ability of virtually self-polymerizing and depositing on virtually any surfaces, has been considered as an effective carbon precursor [24,25]. Our previous work also demonstrated the good coating property of dopamine [26,27]. However, the expensive cost impedes its further practical application. Considering the basic molecular structure of dopamine, it is inferred that separated catechol and polyamine may be utilized to polymerize as the carbon precursor.

Based on this thought, low-cost catechol and polyamine (CPA) is utilized to synthesize N and O dual-doped hollow carbon spheres (DHCSs) as sulfur hosts. It is the first time that the CPA is demonstrated to prepare functional carbon material. There are three main advantages in this work. Firstly, a new carbon precursor is adopted to achieve in-situ doped carbon host. Such carbon precursor can easily form uniform coating layer on the template at room temperature without the requirements of complex equipment or strict reaction conditions, showing its potential application in other field. Most importantly, it is cheaper than dopamine, and equivalent coating ability of CPA as dopamine is found in the experiment. Secondly, N/O dual-doped carbon can be obtained, providing abundance active sites to bond with LiPSs. The influences of co-doping N/O in sulfur-carbon formation and LiPSs adsorption are investigated by the combination of experiment characterization such as X-ray photoelectron spectroscopy (XPS) and theoretical calculation based on first-principle density functional theory (DFT). Thirdly, the conductive carbon with hollow framework can act as a physical confinement to host sulfur species and provide electrochemical reactor at nanoscale to improve sulfur utilization. Benefited from these advantages, the DHCSs, derived from CPA, act as effective hosts for sulfur species, showing a promising application for advanced Li–S batteries.

2. Experimental section

2.1. Sample preparation

2.1.1. Synthesis of SiO_2 spheres

SiO_2 spheres were synthesized according to a slightly modified Stöber method [28]. The typical synthesis process is described as following: Tetraethyl orthosilicate (TEOS) (13.5 mL) was added quickly into a mixture solution of deionized water (70 mL), ethanol (180 mL) and ammonium aqueous (27 mL). After vigorous stirring at room temperature for 3 h, the SiO_2 spheres were isolated by centrifugation and washed using deionized water and ethanol at least three times.

2.1.2. Synthesis of SiO_2@CPA

The as-obtained SiO_2 (0.32 g) spheres were dispersed into deionized water (150 mL) using continuous ultrasonication. Then, catechol (0.3 g) and diethylenetriamine (285 μL) were added to react for 24 h at room temperature. The product was separated by centrifugation and dried in vacuum oven at 80 °C for overnight.

2.1.3. Synthesis of hollow carbon spheres

The carbonization was conducted at 200 °C for 1 h, followed by heating at 700 °C (or 800 °C, or 900 °C) for 3 h with 2 °C min^{-1} in argon atmosphere. Subsequently, the carbonized product was treated with hydrofluoric acid (15%) to remove the SiO_2 template. Finally, the hollow carbon spheres were obtained by centrifugation and dried in freezing dryer. According to the calcination temperatures, the corresponding hollow carbon samples are denoted as DHCSs700, DHCSs800 and DHCSs900, respectively.

2.1.4. Synthesis of carbon/sulfur composites

The melt infiltration is used to impregnate sulfur into the hollow carbon sphere. Both sulfur and as-prepared hollow carbon samples with a certain proportion were mixed via grinding, and then heated at 155 °C for 12 h under argon atmosphere. The obtained composites were designated as S/DHCSs700, S/DHCSs 800 and S/DHCSs900, respectively.

2.2. Cell assembly and electrochemical measurement

The slurry containing 80 wt% as-prepared S/DHCSs, 10 wt% acetylene black and 10 wt% carboxy methyl cellulose (CMC)/styrene butadiene rubber (SBR) (CMC: SBR = 1: 1, mass) was coated onto aluminum foil with doctor blade. After drying at 60 °C overnight in vacuum oven, CR-2032-type coin cells were assembled in an argon-filled glovebox to measure the electrochemical performances. 1 M lithium bis(trifluoromethanesulfonyl)imide (LiTFSI) in 1,3-dioxolane (DOL) and 1,2-dimethoxyethane (DME) (DOL: DME = 1: 1, V/V) was used as electrolyte. The lithium metal foil was used as both counter and reference electrode. The typical sulfur active loading is 1.4 mg cm^{-2} in the cathode. The discharged-charged profiles at different densities from 1.75 V to 2.8 V (vs. Li^+/Li) were conducted on battery system (LAND CT2001A instrument, China). Cyclic voltammetry (CV) curves were obtained on CHI660D at a scan rate of 0.1 mV s^{-1} with voltage range of 1.75–2.8 V. Electrochemical impedance spectra (EIS) were performed on electrochemical workstation (Autolab PGSTAT T302 N) at a frequency range of 0.1 Hz–100 KHz. All electrochemical tests were performed at 25 °C.

2.3. Characterization and measurements

The morphologies of the samples were characterized with scanning electronic microscopy (SEM, HITACHI S-4800) and transmission electron microscope (TEM, TECNAI F30). The crystal structure of all the samples were analyzed with the Rigaku X-ray diffraction (XRD, miniflex600) using Cu-Kα radiation operated at 40 kV and 15 mA. The data were collected in the range from 10° to 60° with scanning speed of 2° min^{-1}. The Raman spectra were performed on Xplora using the 532 nm excitation with the resolution of 1 cm^{-1}. The compositions of the samples were measured on Fourier transform infrared spectrometer (FT-IR, Nicolet IS5 spectrometer). The X-ray Photoelectron spectrum (XPS) was recorded on Qtac-100 Scanning microprobe. The proportion of the element is analyzed with element analysis instrument (Varia-EL-III). The sulfur amount in the composites was determined with

thermal analyzer (SDT-Q600) in nitrogen at 10°/min. Nitrogen adsorption-desorption isotherms were analyzed with ASAP 2020 to get the Brunauer-Emmett-Teller (BET) specific surface area and pore distribution.

2.4. Computational method

Sulfur species (S_8, Li_2S_8, Li_2S_6, Li_2S_4) molecules are calculated by Gaussian 09 to find optimized structures [29,30]. The calculations were carried out at the level of M06-2x/6-311(2d) [31]. Periodic boundary condition were used to model adsorption of polysulfides on carbon surface, N-doped surface, O-doped surface and N/O-doped surface. A (6 × 6) supercell with 72 atoms in the single layer graphite were used to construct the surface. Following the observation of experiments, pyridinic N and quaternary N were chosen. The cut-off energy were set to 400 eV for the calculation of the valence electrons. We chose PAW(projected augmented wave) pseudopotentials for the core electrons [32]. The vacuum above the surface is set to 10 Å, which makes sure that the interactions between surfaces could be ignored. The Monkhorst-Pack procedure are applied to generate k-points sampling with a mesh of 3 × 3 × 1. DFT-D2 were concerned to account for the van der Waals interactions [33]. The above mentioned calculations were performed by Vienna Ab-initio Simulation Package (VASP) with GGA framework [34]. The adsorption energy (ΔE_{ad}) is calculated following Equation (1):

$$\Delta E_{ad} = E(\text{surface/S}) - E(\text{surface}) - E(\text{S}) \quad (1)$$

E(surface/S) accounts for the total energy of the surface with adsorbed polysulfides. E(surface) and E(S) stand for energy of single surface and polysulfides.

3. Results and discussion

3.1. DHCSs characterization

The synthesis process of DHCSs is illustrated in Fig. 1a. First, SiO_2 spheres as sacrificial templates were prepared through traditional Stöber method. The hard-templating method was adopted to prepare hollow structure as the structural parameters of products could be easily controlled by the precursor [35]. Then, the polymer layer, generated from CPA, was easily coated on the surfaces of SiO_2 spheres at room temperature due to the electrostatic interaction between the polymers and SiO_2 (Table S1). After heat treatment, the polymer layer would convert into nitrogen/oxygen dual-doped carbon nanospheres in situ. Finally, the DHCSs with hollow interiors could be readily obtained by etching the SiO_2 templates with hydrofluoric acid solution. Recently, coating polymers layer or fabricating hollow carbon shows wide application in catalysis, energy and biology [35–37]. Our experiment demonstrates that the coating capability of CPA is not only limited on SiO_2 spheres, but also on other material, such as organic polymers (polystyrene, PS), and carbon materials (vapor-grown carbon fiber, VGCF) (Fig. S1). Furthermore, thermogravimetric analysis (TGA) reveals that pure CPA can maintain almost 52% carbon yield in N_2 at 800 °C (Fig. S2). The above results demonstrate that the CPA is a versatile and effective carbon coating precursor, which may offer a new platform for designing carbon layers or hollow carbon materials.

The specific morphologies of the synthetic products are recorded by the scanning electron microscope (SEM) and transmission electron microscope (TEM) images as shown in Fig. 1b–1g. The SEM images (Fig. 1b and Fig. S3) display that the prepared SiO_2 is uniform sphere, confirming its suitability as a template. TEM images in Fig. 1e shows that the initial SiO_2 spheres have smooth surfaces with an average size of 290 nm. After coated on CPA, the surfaces become relatively rough (Fig. 1c). TEM image clearly reveals the existence of CPA on the SiO_2 surface with a uniform shell thickness of 30 nm (Fig. 1f). After etching SiO_2 templates, the spherical morphologies are still well maintained in all samples prepared by different temperatures (Fig. 1d, Fig. S4a, S4b). Obvious interior space can be clearly observed (Fig. 1g, Fig. S4c, S4d), demonstrating the successful synthesis of hollow carbon spheres. Dynamic light scattering (DLS) techniques are carried out to study the dispersion of DHCSs in the aqueous solution. A typical Tyndall effect can be observed (inset Fig. 1d), identifying the very fine suspension of DHCSs in the water, which may be benefited from the rich doped-heteroatoms in the DHCSs. The well distribution of DHCSs promises their widely potential application in other fields, such as supercapacitor, drug delivery and catalysis [38,39].

The structure features of the as-prepared DHCSs (DHCSs700, DHCSs800, and DHCSs900) were characterized by XRD, FT-IR, Raman and BET. As shown in Fig. 2a, all samples exhibit two broad peaks at around 24° and 43°, corresponding to (002) and (001) diffraction planes of graphite, respectively. The broad peaks indicate the amorphous structure of the obtained NHCSs. With rising annealing temperatures, the (002) peak shifts slightly from 23.96° to 24.9°, reflecting a smaller distance of graphitic layers based on Bragg's law (listed in Table S2) [40,41]. The changing distance of graphitic layers may be caused by the release of functional groups with the increase of pyrolysis temperatures, which can be observed from the FTIR spectroscopy (Fig. S5). Furthermore, elemental analysis (Table S3) reveals that the nitrogen content in DHCS700, DHCSs800 and DHCSs900 is 9.74%, 7.05% and 4.46%, respectively. Corresponding calculated oxygen content is 12.75%, 13.98% and 15.54%, respectively.

Raman spectra of the DHCSs are displayed in Fig. 2b. The D band at around 1353 cm^{-1} reflects the disordered carbon structure. While the G band at about 1580 cm^{-1} implies the graphitic feature in carbon materials [42]. With the increasing pyrolysis temperatures, the G band shifts slightly to lower wavenumbers, disclosing an increasing graphitic structure, which is well agreed with the result of XRD data. Nitrogen adsorption-desorption isotherms were measured to obtain the information of the pore structure in DHCSs. As shown in Fig. 2c, The DHCSs obtained at different temperatures combines the type I and IV isotherm based on International Union of Pure and Applied Chemistry (IUPAC) classification [43], suggesting the coexistence of microporosity and mesoporosity. The corresponding mesopore size distribution calculated based on Barrett-Joyner-Halenda (BJH) methodology confirms the mesopore centered at 3.9 nm in all samples (Fig. 2d). Horvath-Kawazoe (HK) method [44] was used to detect the microporous distribution (insert Fig. 2 d). The micropore size has a narrow distribution of 0.53 nm in DHCSs. Such small pore in material has shown beneficial effect on adsorbing LiPSs [45,46]. More textural properties are listed in Table S4. The BET surface areas of DHCSs700, DHCSs800 and DHCSs900 increase from 645 to 851 and 1135 $m^2\ g^{-1}$, and the corresponding total pore volumes raise from 1.03 to 1.47 and 1.74 $m^3\ g^{-1}$, respectively. Associated with the results of XRD, FT-IR and element analysis, the enhancement in BET surface areas and total pore volumes might be attributed to the partial decomposition of functional groups in carbon framework with increasing carbonization temperature [47]. Generally, the electronic conductivity of the carbon has a close relationship with the graphitization degree. A four-contact method was used to analyze the resistivity of the DHCSs powders under the pressure of 4 MPa. As shown in Table S3, the resistance declines from 9.45 Ω cm (DHCSs700) to 0.49 Ω cm (DHCSs800) and 0.17 Ω cm (DHCSs900). Such decrease in resistance would be favorable for the kinetic of the electrochemical reaction.

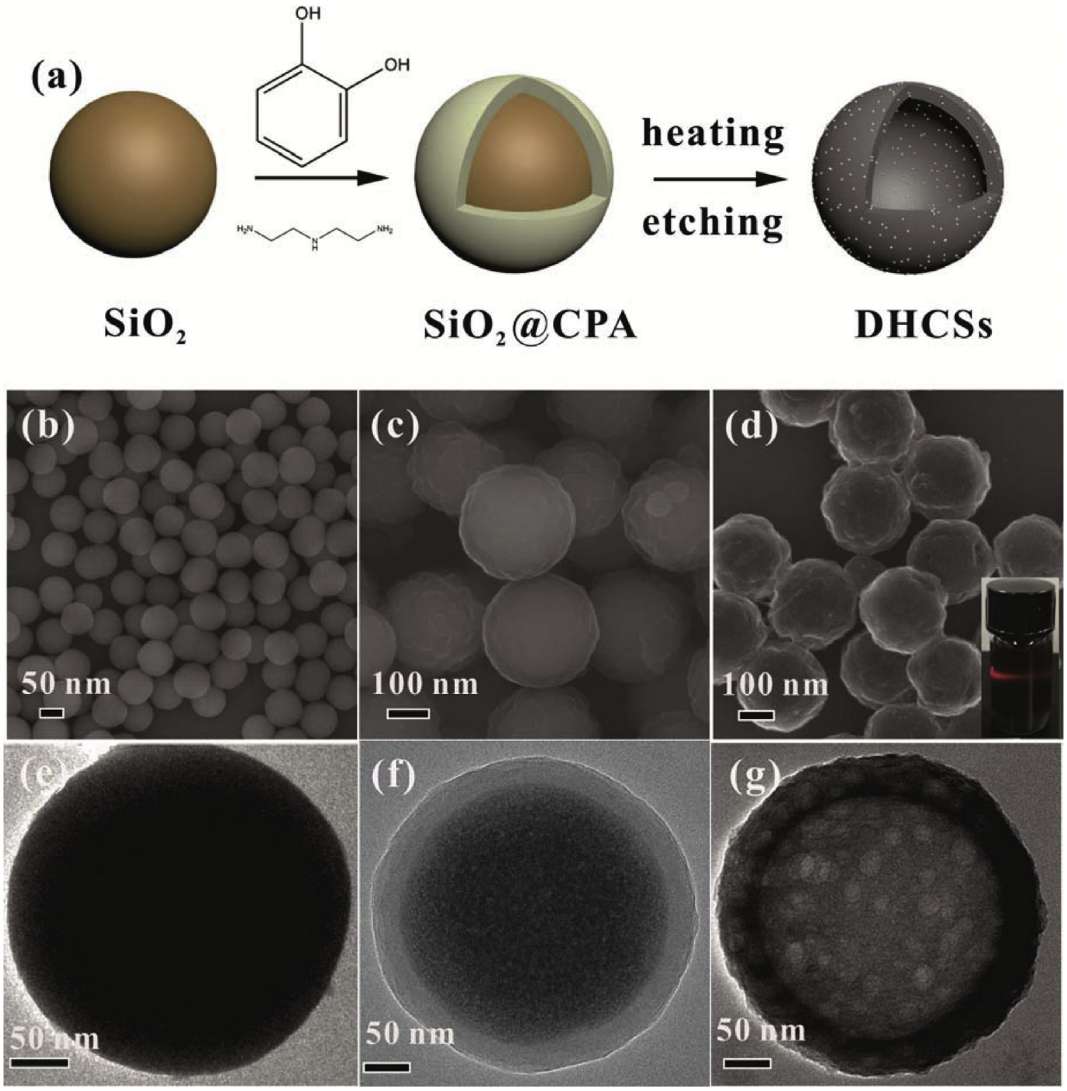

Fig. 1. (a) Schematic illustration for the synthesis process of DHCSs, (b–g) SEM and TEM images of (b, e) SiO_2, (c, f) SiO_2@CPA and (d, g) DHCSs800 (inset: photos of DHCSs800 dispersed in water solution). (A colour version of this figure can be viewed online.)

3.2. S/DHCSs characterization

To obtain S/DHCSs composites, a traditional melt-diffusion method was used to impregnate sulfur into DHCSs. The TGA measurement (Fig. 3a) estimates that the amount of sulfur in S/DHCSs700, S/DHCSs800 and S/DHCSs900 is 65%, 66% and 62%, respectively. Compared with pure sulfur, two obvious temperature region can be seen in the S/DHCSs. The first stage below 280 °C with ~55 wt % of sulfur lost can be attributed to the sulfur in mesopores of the carbon shell. While another ~10 wt% of sulfur is lost until 430 °C, reflecting the existence of sulfur in microporous structure or the inner lining due to the strong interaction between sulfur and carbon matrix [48,49]. Nitrogen adsorption-desorption isotherms of S/DHCSs in Fig. S6a shows that the adsorption volume dramatic decrease after infiltrating sulfur. Corresponding pore size distribution (Fig. S6b) indicates that sulfur is diffused into the micropores and mesopores, remaining with small amount of pores at around 50 nm to buffer volume expansion. Fig. S6c describes the XRD spectra of prepared composites. There are no obvious peaks of sulfur, implying that sulfur particles are highly confined within the interior structure of carbon [50,51]. Raman spectra were also used to confirm the existence state of sulfur in the DHCSs. As shown in Fig. S6d, the pure sulfur powders exhibit strong Raman peaks at 152, 214 and 473 cm^{-1}. However, after impregnating sulfur into DHCS, no characteristic signal of sulfur could be ascribed to sulfur, implying that the DHCSs act as excellent physical host of sulfur [52,53]. SEM and TEM images (Fig. 3b–d and Fig. S7) illustrate that well spherical morphologies are obtained after diffusing sulfur into DHCSs. No obvious sulfur particles could be detected at the DHCSs outside. From the results of TGA, XRD and Raman, it can be deduced that sulfur particles should have been incorporated into the DHCSs. Scanning TEM (STEM) discloses the homogeneous distribution of N and O elements in the carbon framework, and the well confinement of S element within the carbon shell (Fig. 3e–i). Further energy dispersive X-ray (EDX) line scan (Fig. S8) indicates that sulfur is confined in the carbon shell and inner lining of shell [48]. The sufficient contact of sulfur with carbon is favorable for the electron transport, especially considering the insulation nature of sulfur. In addition, the enriched N/O distribution could provide strong

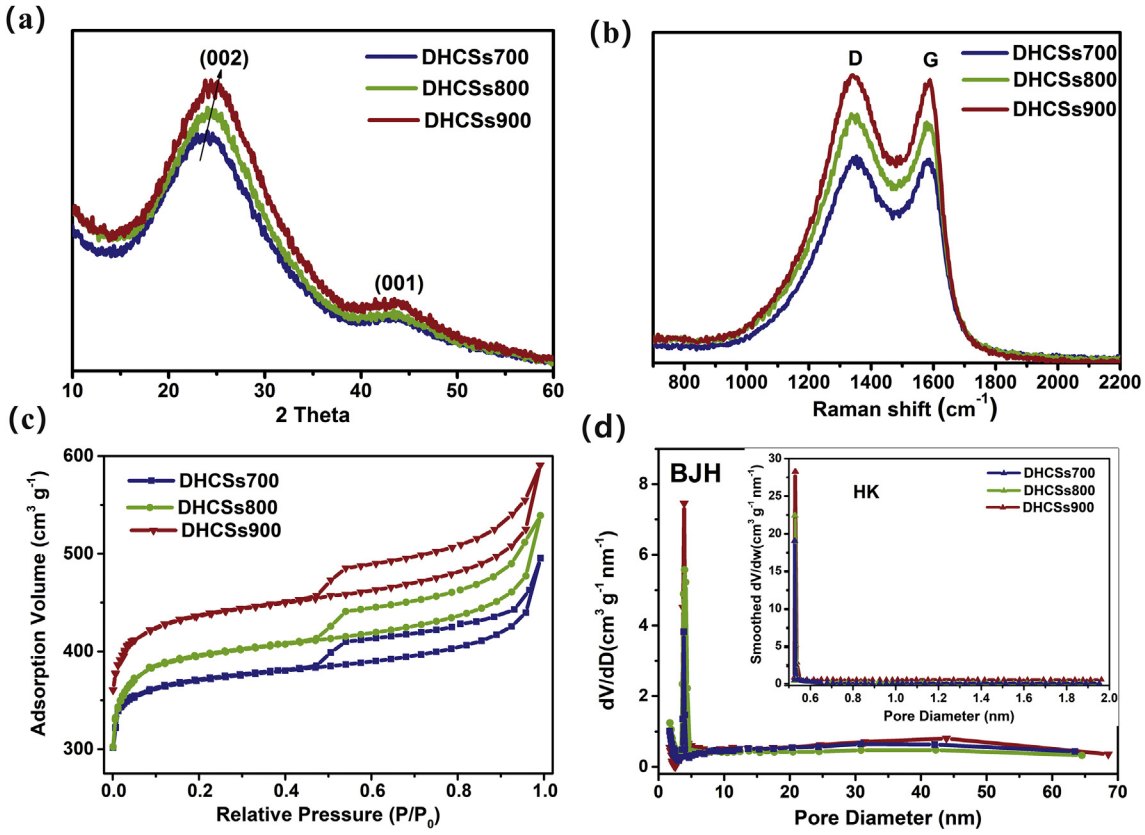

Fig. 2. (a) XRD spectra of DHCSs, (b) Raman spectra of DHCSs, (c) Nitrogen adsorption-desorption isotherms of DHCSs, (d) corresponding mesopore distribution of DHCSs obtained from BJH methodology (inset is the micropore distribution obtained from HK methodology). (A colour version of this figure can be viewed online.)

chemical interaction to anchor LiPSs in the cathode, restraining the shuttle effect and capacity fading. Therefore, it can be seen that the DHCSs act as efficient sulfur hosts, promoting sulfur well diffused into the hollow carbon framework. Each hollow carbon nanosphere can be viewed as a nanoscale electrochemical reaction vessel, providing robust electron pathway, a free-space for accommodating volume expansion and efficient physical/chemical confinement for LiPSs.

3.3. Electrochemical performances

Before testing the electrochemical performances, visible color experiment was carried out to estimate the adsorption ability of as-prepared DHCSs for polysulfides. Li_2S_4 was chosen as a representative of polysulfides. As shown in Fig. S9, there is no obvious change when adding acetylene black. By contrast, the color of Li_2S_4 solution changed from yellow to colorless after adding DHCSs samples, suggesting the strong adsorption of DHCSs for polysulfides.

The specific electrochemical performances of S/DHCSs composites were assessed as cathodes for Li–S batteries. Fig. 4a exhibits the initial cycling voltammetry (CV) profiles of S/DHCSs electrodes at the scanning rate of 0.1 mV S^{-1} within voltage range of 1.75–2.8 V. All curves contain two reductive peaks and one oxidative peak. The first reduced peak at around 2.3 V represents the transformation from solid sulfur to soluble Li_2S_n ($4 \leq n \leq 8$), while the second reduced peak at about 2.0 V belongs to the formation of Li_2S_2/Li_2S. The oxidation peak at roughly 2.4 V reflects the reaction from the final reduced products of Li_2S_2/Li_2S to element sulfur. It should be pointed that with increasing annealing temperatures, the reductive peaks shift to higher voltages while the oxidative peak shifts to lower voltages, which suggests an increased kinetic process and decreased polarization [54]. Fig. 4b displays the first discharge and charge plots of S/DHCSs cathodes at 0.2 C (1 C = 1675 mA g^{-1}). Two typical discharge plateaus can be observed, which are agreed with the results of CV. Higher initial discharge capacity is found in S/DHCSs900, which may be attributed to the higher conductivity and porosity, offering efficient electron pathway and electrolyte diffusion to improve the sulfur utilization. No overcharge phenomenon was observed in the three composites, which might benefit from the doped heteroatoms and the hollow structure. Such structure design plays a physical/chemical confinement for trapping polysulfides dissolution and avoiding shuttle effect. The rate performances of S/DHCSs cathodes were evaluated at different rates. As displayed in Fig. 4c, the S/DHCSs800 delivers the discharge capacity of 1239, 905, 706, 587 and 422 mAh g^{-1} at the current density of 0.1, 0.2, 0.5, 1 and 2 C, respectively. When the current density reverted to 0.1 C, a relative high capacity of 994 mAh g^{-1} could be maintained. The good rate capability of S/DHCSs800 can profile from the moderate value of conductivity and doped atoms.

Fig. 4d presents the cycling performances of S/DHCSs700, S/DHCSs800 and S/DHCSs900 at 0.2 C from 1.75 V to 2.8 V. All cathodes exhibit the similar tendency of capacity change. There is a rapid capacity decline in the initial five cycles, then a slightly rise, finally it keeps a stable platform in the following cycling. Similar results were also observed in the previous studies [18]. After activation via the initial cycling, sulfur species are rearranged and redistributed uniformly in the whole carbon framework. As a result, the improved sulfur utilization could be achieved and the steady

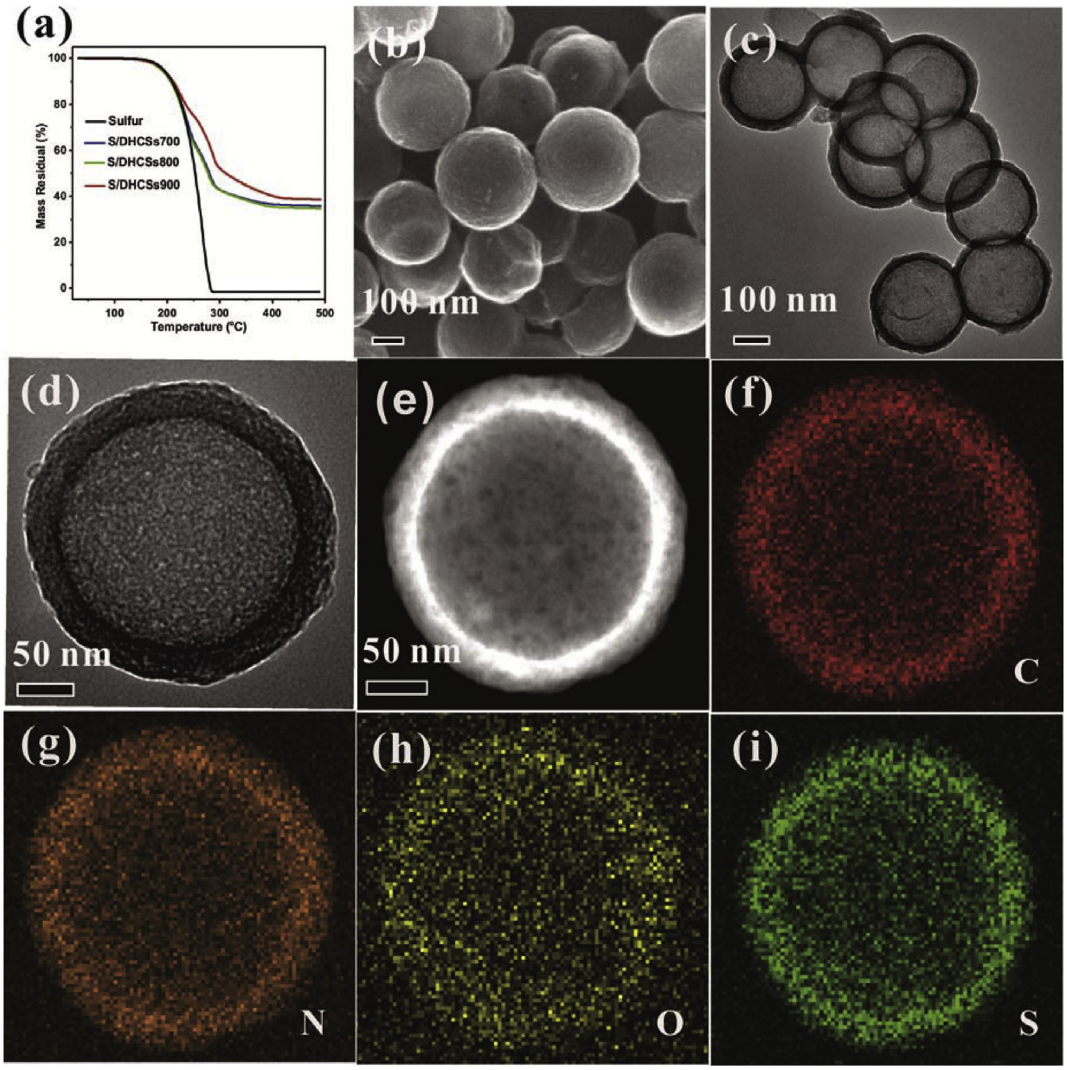

Fig. 3. (a) TGA curves of sulfur and S/DHCSs composites, (b) SEM image of S/DHCSs800, (c) (d) TEM images of S/DHCSs800, (e) STEM image of S/DHCSs800, (f ~ i) corresponding elemental mappings of S/DHCSs800 (f) C (red), (g) N (orange), (h) O (yellow), (i) S (green). (A colour version of this figure can be viewed online.)

discharge capacity was maintained in the subsequent cycles. Though slightly higher initial capacity is obtained for the S/DHCSs900, higher capacity and capacity retention are remained for the S/DHCSs800 (851 mAh g^{-1}/74.3% with ~0.08% capacity decay per cycle after 200 cycles). For practical application, large area mass of cells were assembled to measure the electrochemical performances (Fig. 4e). Through the initial two activation at 0.05 C, the S/DHCSs800 cathode is cycled at 0.5 C for the rest of 700 cycles. Even after long cycling, a typical discharge and charge curves still can be observed (Fig. S10).The excellent cycle stability with 68% capacity retention can be achieved.

3.4. Fundamental mechanism

The above results demonstrate that the DHCSs can act as efficient sulfur hosts for advanced Li–S batteries. To understand the kinetics of the electrochemical reactions during the cycling, ex-situ electrochemical impedance spectra (EIS) of the fresh and the 200th cycled cells were compared as shown in Fig. S11. All Nyquist plots show two semicircles at the high/medium frequency and one inclined line at the low frequency region. The R_e, R_{int} and R_{ct} represent the impedance of electrolyte, the interphase contact between electrode and electrolyte resistance and the charge transfer resistance, respectively [55]. The CPE and W_0 stand for constant phase element and Warburg resistance, respectively. The specific simulating values are listed in Fig. S11c. Before cycling, all samples show similar R_e. The values of R_{int} for the S/DHCSs700, S/DHCSs800 and S/DHCSs900 are 27.02, 16.87 and 15.74 Ω, respectively. The decreasing R_{int} with increasing carbonizing temperature reflects a rising conductivity, in good agreement with the electric resistivity measurement (Table S3). After 200 cycles, the R_e for S/DHCSs800 (4.10 Ω) is smaller than the S/DHCSs700 (6.27 Ω) and S/DHCSs900 (4.72 Ω), implying the less dissolution of high viscous LiPSs into the electrolyte [56]. This is well explained why the S/DHCSs800 has remained the best capacity retention. For each electrode, a decreased tendency in R_{ct} is observed after long cycling, indicating the enhanced reaction kinetics [57]. Associated with cycling measurement, this is due to the rearrangement of sulfur, promoting better contact between active materials and carbon matrix.

For better understanding the advanced electrochemical performances of S/DHCSs, XPS spectra were carried out to explore

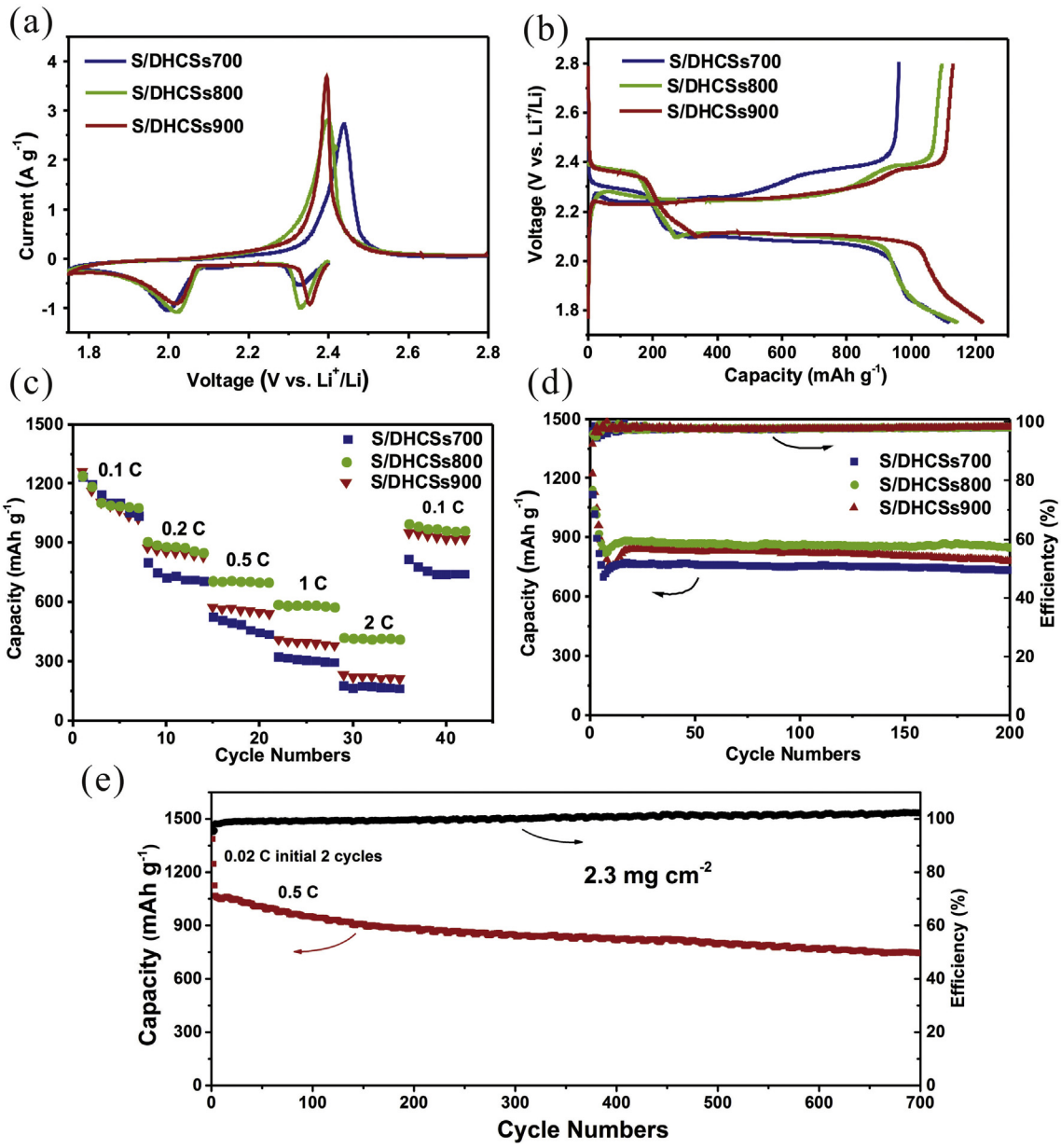

Fig. 4. (a) Initial CV curves of S/DHCSs at 0.1 mV S^{-1}, (b) first discharge and charge profiles of S/DHCSs at 0.2 C, (c) rate performances of S/DHCSs, (d) cycling performances of S/DHCSs at 0.2 C, (e) long cycling performance of S/DHCSs800 at 0.5 C. (A colour version of this figure can be viewed online.)

the structure information of S/DHCSs cathode (Fig. 5 and Fig. S12). Taken the products carbonized at 800 °C for example, the C 1s, N 1s and O 1s signals were detected in both DHCSs800 and S/DHCSs800 (Fig. 5a), confirming the coexistence of N and O in the carbon framework. For the S/DHCSs800, two new peaks at 227.7 eV and 164.4 eV can be observed, which are ascribed to the S 2s and S 2p, respectively. From Fig. 5b and c, it can be found that the O 1s spectrum shifts to lower binding energy, while the N 1s spectrum almost remains the same after impregnating sulfur into the DHCSs. This phenomenon is reflective of the formation of S—O rather than S—N when the N/O dual-doped into the carbon matrix. Because of the higher electronegativity of N (3.04) than C (2.55), the N atom can attract more electron when doped into carbon framework, inducing the nearby O to be polarized and more easily attached by sulfur during the melt-diffusing process [58]. Carefully deconvoluting the O 1s spectrum (Fig. S12a, S12c), three different peaks attributed to O═C, O—C, and C—OH can be detected in both DHCSs800 and S/DHCSs800 [39,59]. The XPS spectrum of N 1s (Fig. S12b, S12d) can be divided into three peaks of 398.6, 400.8 and 403.6 eV, belonging to pyridinic nitrogen (pd-N), pyrrolic nitrogen (pl-N) and quaternary nitrogen (q-N), respectively. In Fig. 5d, it can be clearly seen that the types of pd-N and pl-N are dominant in the composites. Previous DFT calculations have revealed that pd-N and pl-N can provide strong binding energy with LiPSs to effectively anchor the soluble LiPSs [60], which will also be confirmed in the following calculation. The C 1s spectrum (Fig. 5e) can be deconvoluted into four peaks at 284.8 eV (C—C/C═C), 285.6 eV (C—O/C—N/C—S), 286.6 eV (C—N—C) and 287.0 eV (C═O) [61,62]. The C—S bonding is believed to be formed during the high temperature (155 °C),

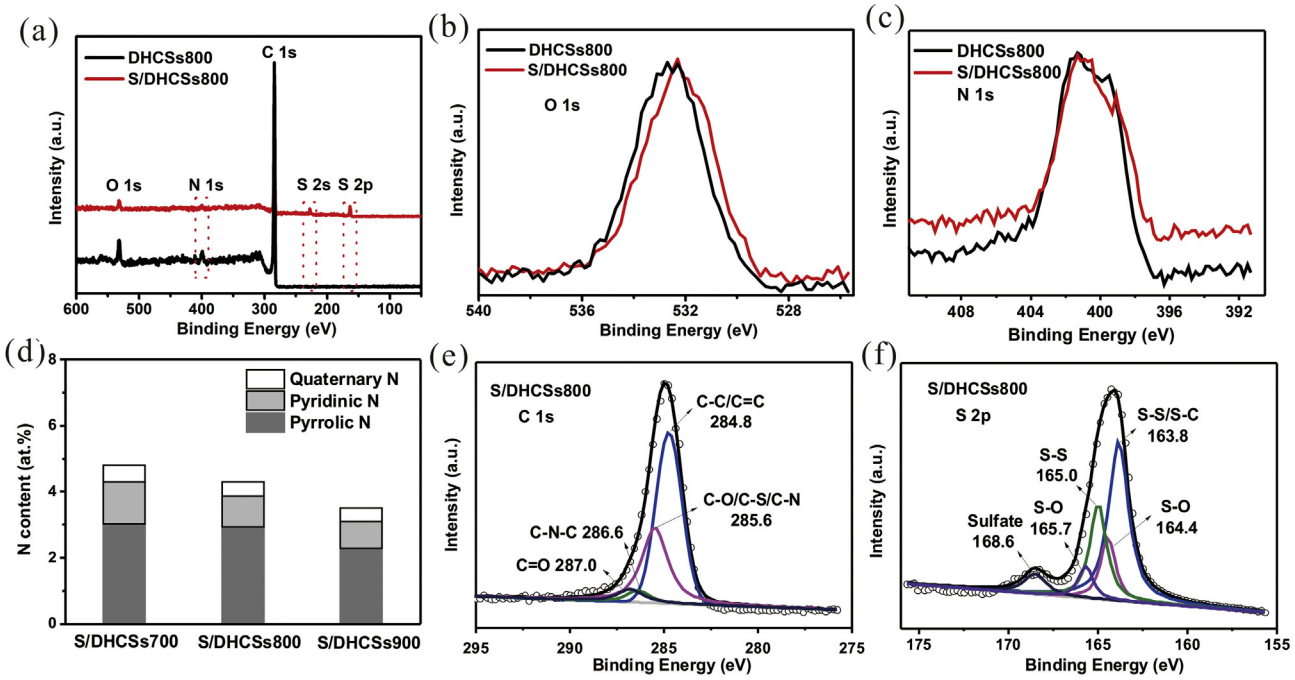

Fig. 5. (a) Survey XPS spectra of DHCSs800 and S/DHCSs800, (b) O 1s of DHCSs800 and S/DHCSs800, (c) N 1S of DHCSs800 and S/DHCSs800, (d) N contents in S/DHCSs, (e) the C 1s of S/DHCSs800, (f) S 2p of S/DHCSs800. (A colour version of this figure can be viewed online.)

which is benefited from the incorporation of N/O heteroatoms [18]. For the S spectrum (Fig. 5f), the S–S/S–C bonds at 163.8 eV, S–O bond at 164.4 eV and 165.7 eV, S–S bond at 165.0 eV, and the sulfate species at 168.6 eV can be obtained after careful deconvolution [18,63]. The sulfate species are detected due to the inevitable oxidation of sulfur in the air. The presence of S–C and S–O bond is consistent with the C 1s and O 1s spectrum, further demonstrating the strong interaction of S with C and O in carbon matrix.

To get further insight into the dual-doped effect, the first principle calculations were conducted to examine the chemical bonding between LiPSs and heteroatom-doped carbon matrix. The specific calculations are described in the experimental section. To confirm the synthetic effect of N/O, the adsorption energy (ΔE_{ad}) of different sulfur species (S_8, Li_2S_8, Li_2S_6 and Li_2S_4) on different doped carbons (N-doped, O-doped, N/O-doped and pure carbon) are calculated. Higher absolute value of ΔE_{ad} reflects stronger interaction between sulfur species and carbon matrix. From the XPS analysis, the pd-N and cyclic O were used to model the CPA-derived carbon. Also, the pd-N and q-N doped carbon are used to compare the chemisorption of different types of N-doping for LiPSs. Fig. 6 and Fig. S13 exhibit the optimized geometric configurations and calculated ΔE_{ad} for sulfur species adsorbed on the different doped carbon surfaces. For the pristine carbon, the lowest ΔE_{ad} is found for all sulfur species, showing the poor affinity of non-polar carbon for LiPSs. After doped with pd-N, q-N or O or N/O, the ΔE_{ad} is enhanced for all types of sulfur species. This result indicate the important role of O, which can help charge redistribution in N doped carbon matrix, facilitating the electron deficient Li more easily to be adsorbed on the carbon matrix [64]. It should be noticed that higher ΔE_{ad} is achieved by the pd-N than the q-N, suggesting that the prepared DHCSs, derived from CPA, act as efficient sulfur hosts due to the dominant pd-N in the carbon matrix from XPS analysis. Most importantly, when the N and O atoms are co-doped into carbon, the greatest ΔE_{ad} can be achieved in all cases of sulfur species, demonstrating the improved chemisorption for dual-doping. Our calculation results also well agree with previous reports, revealing the co-doped carbon is a promising candidate to enhance the interaction with LiPSs [65]. It is puzzled to find that the role of O is often ignored though the fact that O atom is generally found co-existed in single- or dual-heteroatoms doping [39]. Therefore, the synergistic effect of N/O co-doping should be brought to the forefront.

4. Conclusion

In conclusion, the N/O dual-doped hollow carbon materials, derived from a new carbon precursor of CPA, are applied as sulfur hosts for Li–S batteries. The CPA can be easily and uniformly coated on the template at room temperature without any surfactant. The obtained S/DHCSs800 exhibits improved rate performance and good cycling stability with the discharge capacity of 851 mAh g^{-1} and small capacity decay of 0.08% per cycle at 0.2 C after 200 cycles. The excellent electrochemical performance could attribute to the synergistic effect of the well-designed hollow structure and the N/O dual doping. The hollow structure could confine sulfur species in the interior hollow at physical scale. XPS reveals the formation of S–O and S–C bond during heating diffusion, assisting trapping sulfur species on the carbon matrix. Further theory calculation demonstrates that the doped N/O atoms could provide stronger chemical interaction with LiPSs than single doping. In addition, it is the first time that the CPA is reported to synthesize carbon material. The CPA exhibits a versatile and effective coating capacity on various templates. The strategy of using CPA as a carbon precursor opens a new platform for designing carbon materials or coating layer.

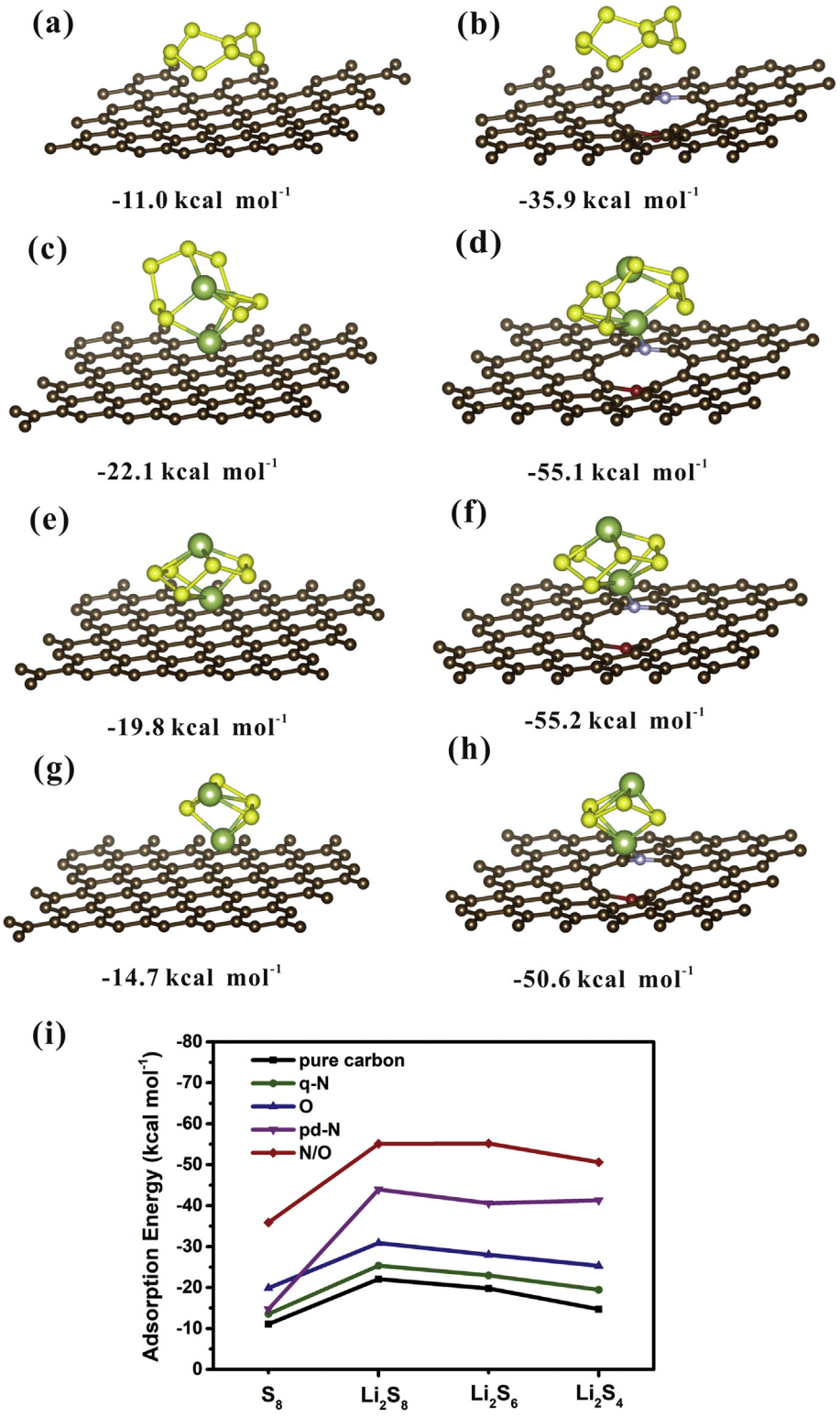

Fig. 6. Optimized molecular configuration and corresponding calculated adsorption energy of polysulfides on (a, c, e, g) pure carbon surface, and (b ~ h) N/O dual-doped carbon surfaces, (i) comparison of calculated adsorption energy of polysulfides on different doped-carbon. (A colour version of this figure can be viewed online.)

Acknowledgements

The authors gratefully appreciate financial support from the National Natural Science Foundation of China (Grant No.2127318 and No.21321062) and National Found for Fostering Talents of Basic Science (J1310024). The authors also wish to express their thanks to Prof. Daiwei Liao for his valuable suggestions.

Appendix A. Supplementary data

Supplementary data related to this article can be found at http://dx.doi.org/10.1016/j.carbon.2017.08.035.

References

[1] P.G. Bruce, S.A. Freunberger, L.J. Hardwick, J.M. Tarascon, Li-O_2 and Li-S batteries with high energy storage, Nat. Mater. 11 (2012) 19–29.
[2] A. Manthiram, Y. Fu, S.H. Chung, C. Zu, Y.S. Su, Rechargeable lithium-sulfur batteries, Chem. Rev. 114 (23) (2014) 11751–11787.
[3] S. Chen, X. Huang, H. Liu, B. Sun, W. Yeoh, K. Li, et al., 3D hyperbranched hollow carbon nanorod architectures for high-performance lithium-sulfur batteries, Adv. Energy Mater. 4 (8) (2014) 1301761–1301770.
[4] X. Ji, K.T. Lee, L.F. Nazar, A highly ordered nanostructured carbon-sulphur cathode for lithium-sulphur batteries, Nat. Mater. 8 (6) (2009) 500–506.
[5] Y. Zhang, K. Li, J. Huang, Y. Wang, Y. Peng, H. Li, J. Wang, J. Zhao, Preparation of monodispersed sulfur nanoparticles-partly reduced graphene oxide-polydopamine composite for superior performance lithium-sulfur battery, Carbon 114 (2017) 8–14.
[6] J. He, Y. Chen, W. Lv, K. Wen, C. Xu, W. Zhang, et al., Three-Dimensional CNT/graphene–Li_2S aerogel as freestanding cathode for high-performance Li–S batteries, ACS Energy Lett. 1 (4) (2016) 820–826.
[7] L. Zhou, T. Huang, A. Yu, Three-Dimensional flower-shaped activated porous carbon/sulfur composites as cathode materials for lithium–sulfur batteries, ACS Sustain. Chem. Eng. 2 (10) (2014) 2442–2447.
[8] G. Zheng, Y. Yang, J.J. Cha, S.S. Hong, Y. Cui, Hollow carbon nanofiber-encapsulated sulfur cathodes for high specific capacity rechargeable lithium batteries, Nano Lett. 11 (10) (2011) 4462–4467.
[9] X. Tao, J. Wang, Z. Ying, Q. Cai, G. Zheng, Y. Gan, et al., Strong sulfur binding with conducting Magneli-phase Ti(n)O_2(n-1) nanomaterials for improving lithium-sulfur batteries, Nano Lett. 14 (9) (2014) 5288–5294.
[10] Q. Pang, X. Liang, C. Kwok, L.F. Nazar, Review—the importance of chemical interactions between sulfur host materials and lithium polysulfides for advanced lithium-sulfur batteries, J. Electrochem. Soc. 162 (14) (2015) A2567–A2576.
[11] L. Zhou, X. Lin, T. Huang, A. Yu, Nitrogen-doped porous carbon nanofiber webs/sulfur composites as cathode materials for lithium-sulfur batteries, Electrochim. Acta 116 (2014) 210–216.
[12] C.P. Yang, Y.X. Yin, H. Ye, K.C. Jiang, J. Zhang, Y.G. Guo, Insight into the effect of boron doping on sulfur/carbon cathode in lithium-sulfur batteries, ACS Appl. Mater. Interfaces 6 (11) (2014) 8789–8795.
[13] B. Papandrea, X. Xu, Y. Xu, C.-Y. Chen, Z. Lin, G. Wang, et al., Three-dimensional graphene framework with ultra-high sulfur content for a robust lithium–sulfur battery, Nano Res. 9 (1) (2016) 240–248.
[14] F. Sun, J. Wang, H. Chen, W. Li, W. Qiao, D. Long, et al., High efficiency immobilization of sulfur on nitrogen-enriched mesoporous carbons for Li-S batteries, ACS Appl. Mater. Interfaces 5 (12) (2013) 5630–5638.
[15] X. Wang, T. Gao, F. Han, Z. Ma, Z. Zhang, J. Li, C. Wang, Stabilizing high sulfur loading Li–S batteries by chemisorption of polysulfide on three-dimensional current collector, Nano Energy 30 (2016) 700–708.
[16] F. Wu, J. Li, Y. Tian, Y. Su, J. Wang, W. Yang, et al., 3D coral-like nitrogen-sulfur co-doped carbon-sulfur composite for high performance lithium-sulfur batteries, Sci. Rep. 5 (2015) 13340–13350.
[17] Q. Pang, J. Tang, H. Huang, X. Liang, C. Hart, K.C. Tam, L.F. Nazar, A Nitrogen and Sulfur Dual-doped Carbon derived from Polyrhodanine@Cellulose for advanced lithium-sulfur batteries, Adv. Mater. 27 (2015) 6021–6228.
[18] K. Mi, S. Chen, B. Xi, S. Kai, Y. Jiang, J. Feng, et al., Sole chemical confinement of polysulfides on nonporous nitrogen/oxygen dual-doped carbon at the kilogram scale for lithium-sulfur batteries, Adv. Funct. Mater. 27 (1) (2016) 1–13.
[19] V. Perazzolo, C. Durante, R. Pilot, A. Paduano, J. Zheng, G.A. Rizzi, et al., Nitrogen and sulfur doped mesoporous carbon as metal-free electrocatalysts for the in situ production of hydrogen peroxide, Carbon 95 (2015) 949–963.
[20] H. Chen, Y. Xiong, T. Yu, P. Zhu, X. Yan, Z. Wang, et al., Boron and nitrogen co-doped porous carbon with a high concentration of boron and its superior capacitive behavior, Carbon 113 (2017) 266–273.
[21] X. Wang, M. Lou, X. Yuan, W. Dong, C. Dong, H. Bi, et al., Nitrogen and oxygen dual-doped carbon nanohorn for electrochemical capacitors, Carbon 118 (2017) 511–516.
[22] S. Li, Y. Liang, D. Wu, R. Fu, Fabrication of bimodal mesoporous carbons from petroleum pitch by a one-step nanocasting method, Carbon 48 (3) (2010) 839–843.
[23] Y. Wu, E. Rahm, R. Holze, Effects of heteroatoms on electrochemical performance of electrode materials for lithium ion batteries, Electrochim. Acta 47 (21) (2002) 3491–3507.
[24] R. Liu, S.M. Mahurin, C. Li, R.R. Unocic, J.C. Idrobo, H. Gao, et al., Dopamine as a carbon source: the controlled synthesis of hollow carbon spheres and yolk-structured carbon nanocomposites, Angew. Chem. Int. Ed. 50 (30) (2011) 6799–6802.
[25] H. Lee, S.M. Dellatore, W.M. Miller, P.B. Messersmith, Mussel-inspired surface chemistry for multifunctional coatings, Science 318 (5849) (2007) 426–430.
[26] J. Dai, C. Shi, C. Li, X. Shen, L. Peng, D. Wu, et al., A rational design of separator with substantially enhanced thermal features for lithium-ion batteries by the polydopamine–ceramic composite modification of polyolefin membranes, Energy Environ. Sci. 9 (10) (2016) 3252–3261.
[27] C. Shi, J. Dai, S. Huang, C. Li, X. Shen, P. Zhang, et al., A simple method to prepare a polydopamine modified core-shell structure composite separator for application in high-safety lithium-ion batteries, J. Membr. Sci. 518 (2016) 168–177.
[28] W. Stöber, A. Fink, E. Bohn, Controlled growth of monodisperse silica spheres in the micron size range, J. Colloid Interface Sci. 26 (1) (1968) 62–69.
[29] R. Krishnan, J.S. Binkley, R. Seeger, J.A. Pople, Self-consistent molecular orbital methods. XX. A basis set for correlated wave functions, J. Chem. Phys. 72 (1) (1980) 650–654.
[30] A. McLean, G. Chandler, Contracted Gaussian basis sets for molecular calculations. I. Second row atoms, Z= 11–18, J. Chem. Phys. 72 (10) (1980) 5639–5648.
[31] Y. Zhao, D.G. Truhlar, The M06 suite of density functionals for main group thermochemistry, thermochemical kinetics, noncovalent interactions, excited states, and transition elements: two new functionals and systematic testing of four M06-class functionals and 12 other functionals, Theor. Chem. Acc. 120 (1) (2008) 215–241.
[32] P.E. Blöchl, Projector augmented-wave method, Phys. Rev. B 50 (24) (1994) 17953–17979.
[33] S. Grimme, Semiempirical GGA-type density functional constructed with a long-range dispersion correction, J. Comput. Chem. 27 (15) (2006) 1787–1799.
[34] G. Kresse, J. Furthmüller, Efficient iterative schemes for ab initio total-energy calculations using a plane-wave basis set, Phys. Rev. B 54 (16) (1996) 11169–11186.
[35] X. Lai, J.E. Halpert, D. Wang, Recent advances in micro-/nano-structured hollow spheres for energy applications: from simple to complex systems, Energy Environ. Sci. 5 (2) (2012) 5604–5618.
[36] W.X. Mao, X.J. Lin, W. Zhang, Z.X. Chi, R.W. Lyu, A.M. Cao, et al., Core-shell structured TiO2@polydopamine for highly active visible-light photocatalysis, Chem. Commun. 52 (44) (2016) 7122–7125.
[37] M. Gürsoy, M. Karaman, Surface Treatments for Biological, Chemical and Physical Applications, John Wiley & Sons, 2016.
[38] A.M. De Campos, A. Sánchez, M.A.J. Alonso, Chitosan nanoparticles: a new vehicle for the improvement of the delivery of drugs to the ocular surface. Application to cyclosporin A, Int. J. Pharm. 224 (1) (2001) 159–168.
[39] F. Pei, T. An, J. Zang, X. Zhao, X. Fang, M. Zheng, Q. Dong, N. Zheng, From hollow carbon spheres to N-Doped hollow porous carbon bowls: rational design of hollow carbon host for Li-S batteries, Adv. Energy Mater. (2016) 6.
[40] X. Liu, C. Giordano, M. Antonietti, A facile molten-salt route to graphene synthesis, Small 10 (1) (2014) 193–200.
[41] X.-H. Li, J. Zhang, X. Chen, A. Fischer, A. Thomas, M. Antonietti, et al., Condensed graphitic carbon nitride nanorods by nanoconfinement: promotion of crystallinity on photocatalytic conversion, Chem. Mater. 23 (19) (2011) 4344–4348.
[42] F. Tuinstra, J.L. Koenig, Raman spectrum of graphite, J. Chem. Phys. 53 (3) (1970) 1126–1130.
[43] T.J. Barton, L.M. Bull, W.G. Klemperer, D.A. Loy, B. McEnaney, M. Misono, et al., Tailored porous materials, Chem. Mater. 11 (10) (1999) 2633–2656.
[44] G. Horvath, K. Kawazoe, Method for the calculation of effective pore size distribution in molecular sieve carbon, J. Chem. Eng. Jpn. 16 (6) (1983) 470–475.
[45] Z. Wei Seh, W. Li, J.J. Cha, G. Zheng, Y. Yang, M.T. McDowell, P.-C. HSu, Y. Cui, Sulphur–TiO_2 yolk–shell nanoarchitecture with internal void space for long-cycle lithium–sulphur batteries, Nat. Commun. 4 (2013) 1331–1337.
[46] N. Jayaprakash, J. Shen, S.S. Moganty, A. Corona, L.A. Archer, Porous hollow Carbon@Sulfur composites for high-power lithium-sulfur batteries, Angew. Chem. Int. Ed. 50 (26) (2011) 5904–5908.
[47] D. Zheng, C. Huang, X. Wang, Post-annealing reinforced hollow carbon nitride nanospheres for hydrogen photosynthesis, Nanoscale 7 (2) (2015) 465–470.
[48] G. He, S. Evers, X. Liang, M. Cuisinier, A. Garsuch, L.F. Nazar, Tailoring porosity in carbon nanospheres for lithium–sulfur battery cathodes, ACS Nano 7 (12) (2013) 10920–10930.
[49] C. Liang, N.J. Dudney, J.Y. Howe, Hierarchically structured sulfur/carbon nanocomposite material for high-energy lithium battery, Chem. Mater. 21 (19) (2009) 4724–4730.
[50] R. Elazari, G. Salitra, A. Garsuch, A. Panchenko, D. Aurbach, Sulfur-impregnated activated carbon fiber cloth as a binder-free cathode for rechargeable Li-S batteries, Adv. Mater. 23 (47) (2011) 5641–5644.
[51] B. Zhang, X. Qin, G.R. Li, X.P. Gao, Enhancement of long stability of sulfur cathode by encapsulating sulfur into micropores of carbon spheres, Energy Environ. Sci. 3 (10) (2010) 1531–1537.
[52] G. Hu, Z. Sun, C. Shi, R. Fang, J. Chen, P. Hou, et al., A sulfur-rich Copolymer@CNT hybrid cathode with dual-confinement of polysulfides for high-performance lithium-sulfur batteries, Adv. Mater. (2016) 1603835–1603841.
[53] G. Zhou, D.-W. Wang, F. Li, P.-X. Hou, L. Yin, C. Liu, et al., A flexible nanostructured sulphur–carbon nanotube cathode with high rate performance for Li-S batteries, Energy Environ. Sci. 5 (10) (2012) 8901–8906.
[54] Y. Peng, B. Li, Y. Wang, X. He, J. Huang, J. Zhao, Prussian blue: a potential material to improve the electrochemical performance of lithium-sulfur batteries, ACS Appl. Mater. Interfaces 9 (2017) 4397–4403.
[55] Z. Deng, Z. Zhang, Y. Lai, J. Liu, J. Li, Y. Liu, Electrochemical impedance spectroscopy study of a lithium/sulfur battery: modeling and analysis of capacity

fading, J. Electrochem. Soc. 160 (4) (2013) A553–A558.
[56] C. Zu, Y.S. Su, Y. Fu, A. Manthiram, Improved lithium-sulfur cells with a treated carbon paper interlayer, Phys. Chem. Chem. Phys. 15 (7) (2013) 2291–2297.
[57] Z.-L. Xu, J.-Q. Huang, W.G. Chong, X. Qin, X. Wang, L. Zhou, et al., In situ TEM study of volume expansion in porous carbon nanofiber/sulfur cathodes with exceptional high-rate performance, Adv. Energy Mater. (2017) 1602078–1602099.
[58] J. Song, T. Xu, M.L. Gordin, P. Zhu, D. Lv, Y.-B. Jiang, et al., Nitrogen-doped mesoporous carbon promoted chemical adsorption of sulfur and fabrication of high-areal-capacity sulfur cathode with exceptional cycling stability for lithium-sulfur batteries, Adv. Funct. Mater. 24 (9) (2014) 1243–1250.
[59] G. Zhou, L.-C. Yin, D.-W. Wang, L. Li, S. Pei, I.R. Gentle, et al., Fibrous hybrid of graphene and sulfur nanocrystals for high-performance lithium–sulfur batteries, ACS Nano 7 (6) (2013) 5367–5375.
[60] L.-C. Yin, J. Liang, G.-M. Zhou, F. Li, R. Saito, H.-M. Cheng, Understanding the interactions between lithium polysulfides and N-doped graphene using density functional theory calculations, Nano Energy 25 (2016) 203–210.
[61] L. Chai, J. Wang, H. Wang, L. Zhang, W. Yu, L. Mai, Porous carbonized graphene-embedded fungus film as an interlayer for superior Li–S batteries, Nano Energy 17 (2015) 224–232.
[62] G. Zhou, E. Paek, G.S. Hwang, A. Manthiram, Long-life Li/polysulphide batteries with high sulphur loading enabled by lightweight three-dimensional nitrogen/sulphur-codoped graphene sponge, Nat. Commun. 6 (2015) 7760–7770.
[63] W. Li, Z. Zhang, W. Kang, Y. Tang, C.-S. Lee, Rice-like sulfur/polyaniline nanorods wrapped with reduced graphene oxide nanosheets as high-performance cathode for lithium-sulfur batteries, ChemElectroChem 3 (6) (2016) 999–1005.
[64] J.-J. Chen, R.-M. Yuan, J.-M. Feng, Q. Zhang, J.-X. Huang, G. Fu, M.-S. Zheng, B. Ren, Q.-F. Dong, Conductive lewis base matrix to recover the missing link of Li_2S_8 during the sulfur redox cycle in Li–S battery, Chem. Mater. 27 (6) (2015) 2048–2055.
[65] T.Z. Hou, X. Chen, H.J. Peng, J.Q. Huang, B.Q. Li, Q. Zhang, et al., Design principles for heteroatom-doped nanocarbon to achieve strong anchoring of polysulfides for lithium-sulfur batteries, Small 12 (24) (2016) 3283–3291.